Building Change Detection From Multitemporal High-Resolution Remotely Sensed Images Based on a Morphological Building Index

Xin Huang, *Member, IEEE*, Liangpei Zhang, *Senior Member, IEEE*, and Tingting Zhu

***Abstract*—In this study, urban building change detection is investigated, considering that buildings are one of the most dynamic structures in urban areas. To this aim, a novel building change detection approach for multitemporal high-resolution images is proposed based on a recently developed morphological building index (MBI), which is able to automatically indicate the presence of buildings from high-resolution images. In the MBI-based change detection framework, the changed building information is decomposed into MBI, spectral, and shape conditions. A variation of the MBI is a basic condition for the indication of changed buildings. Besides, the spectral information is used as a mask since the change of buildings is primarily related to the spectral variation, and the shape condition is then used as a post-filter to remove irregular structures such as noise and road-like narrow objects. The change detection framework is carried out based on a threshold-based processing at both the feature and decision levels. The advantages of the proposed method are that it does not need any training samples and it is capable of reducing human labor, considering the fact that the current building change detection methods are totally reliant on visual interpretation. The proposed method is evaluated with a QuickBird dataset from 2002 and 2005 covering Hongshan District of Wuhan City, China. The experiments show that the proposed change detection algorithms can achieve satisfactory correctness rates (over 80%) with a low level of total errors (less than 10%), and give better results than the supervised change detection using the support vector machine (SVM).**

***Index Terms*—Building index, change detection, high resolution, morphological, multitemporal, urban.**

I. Introduction

CHANGE detection is one of the most important techniques for remote sensing applications. It provides essential information for decision making in the monitoring of land use, design of the urban landscape, assessment of regional environments, and rapid response to damaging events. The traditional change detection techniques are built on low- or medium-resolution remotely sensed images. The traditional methods therefore always refer to pixel-based radiometric difference between multitemporal images, due to the limitations of the spatial resolution. In recent years, with the increasing availability of high-resolution data, it is possible to identify detailed changes occurring at the level of ground structures such as buildings [1]. However, the development of high-resolution Earth Observation techniques poses challenges to the traditional change detection methods. Conventional change detection techniques become ineffective on high-resolution images due to the following factors:

1) Pixel-based radiometric or spectral information is not adequate for the representation of the geometrical and textural information present in high-resolution images [2].
2) Pixel-based or radiometric-based change detection methods are subject to a large number of false alarms when applied to high-resolution images, due to the effects of scene illumination, sensor view angles and the residual misregistration between multitemporal images [3].

To solve these problems, spatial approaches that consider the spatial dependence among neighboring pixels, e.g., object, textural or structural-based image description, have been proposed for high-resolution image change detection. Gueguen *et al.* [1] applied top-hat transformation to multitemporal high-resolution images in order to detect internally displaced people camps after the Haiti earthquake. Im *et al.* [4] proposed an object-based change detection method based on image segmentation and correlation image analysis techniques. The idea is based on the fact that pairs of brightness values from the same geographic region (e.g., an object) between multitemporal images tend to be highly correlated for no change and uncorrelated for change. Bovolo [5] proposed a multilevel object-based change vector analysis (CVA) approach, where the change information in multiple segmentation scales was integrated. Berberoglu *et al.* [6] evaluated CVA with and without image texture derived from the co-occurrence matrix and a variogram for detecting land use/cover change. In the experiment it was found that the spectral bands together with the variogram yielded the most accurate results. Dalla Mura *et al.* [7] proposed to integrate morphological filters and the CVA technique for high-resolution image change detection. Their experiments validated the effectiveness of the proposed method in detecting changed areas in a more accurate way than with the traditional pixel-based CVA technique. Pagot and Pesaresi [8] conducted a comparative study of urban post-conflict change classification using a series of spectral and structural features in a support vector machine (SVM). Robertson

Manuscript received October 03, 2012; revised November 12, 2012; accepted March 03, 2013. Date of publication April 26, 2013; date of current version December 18, 2013. This work was supported in part by the National Natural Science Foundation of China under Grants 41101336, in part by the Program for New Century Excellent Talents in University of China under Grant NCET-11-0396, and in part by the Research Fund for the Doctoral Program of Higher Education of China under Grant 20110141120072.

The authors are with the State Key Laboratory of Information Engineering in Surveying, Mapping and Remote Sensing, Wuhan University, Wuhan 430079, China (e-mail: huang_whu@163.com).

Color versions of one or more of the figures in this paper are available online at http://ieeexplore.ieee.org.

Digital Object Identifier 10.1109/JSTARS.2013.2252423

and King [9] compared pixel- and object-based classification in land-cover change mapping, and it was revealed that the object-based approach depicted change information more accurately than the pixel-based approach. Pacifici *et al.* [10] proposed an innovative neural-net method for change detection from high-resolution optical satellite imagery, called NAHIRI (neural architecture for high-resolution imagery). The NAHIRI model is an improved version of the post-classification comparison, which introduces another neural network as a change mask. Chini *et al.* [11] further improved the NAHIRI system by taking into account the classification uncertainty. More recently, Pacifici and Del Frate [12] developed an automatic change detection method in very-high-resolution images with pulse-coupled neural networks (PCNN). The basic idea is to compare the PCNN signals of the multitemporal images, and a correlation function is then used to measure the similarity of the multitemporal outputs of PCNN.

Although some efforts have been devoted to the development of high-resolution change detection techniques, little attention has been devoted to change detection for a specific target of interest. In this case, target-specific rules or filtering can be integrated into the change detection by analyzing the spectral and structural characteristics of the target. In this study, the building change detection from multitemporal high-resolution images is focused on the consideration that buildings are one of the most dynamic urban structures. Especially in a developing country such as China, knowledge of the construction and removal of buildings is important information for the government, and, hence, the change detection and database updating of urban buildings is one of the major tasks for the regional departments of land and resources. However, building change detection currently relies on human visual interpretation and manual manipulation. In order to alleviate the intensity of manual work and enhance the automation of change detection, we propose an innovative framework for urban building change detection from multitemporal high-resolution images. The method is based on a recently developed morphological building index (MBI) that is able to automatically indicate the presence of buildings from high-resolution imagery [13], [14]. The main advantage of MBI is that it is an unsupervised building index, i.e., it can be implemented without any training samples. Based on the MBI, the building change information is represented by the following three conditions.

1) MBI condition: The MBI is used to highlight the building change areas and filter out other urban structures such as roads, vegetation, and water bodies.
2) Spectral condition: The change of buildings should also be related to spectral variation; therefore, the spectral change is used as a mask.
3) Shape condition: The shape information is utilized as a post-filter in order to reduce false alarms such as small noise and road-like narrow structures.

The performances of the three conditions are discussed and analyzed in the experiments. The QuickBird Wuhan 2002–2005 dataset is used to validate the building change detection algorithms. The rest of the paper is organized as follows. Section II describes the MBI operator and the proposed change detection framework. The multitemporal high-resolution datasets are introduced in Section III. Section IV discusses the experimental results, as well as a comparative study with the SVM-based supervised change detection. Section V concludes the paper.

II. Methodology

A. Morphological Building Index (MBI)

The basic idea of MBI is to build a relationship between the spectral-spatial characteristics of buildings (e.g., brightness, size, and contrast) and the morphological operators (e.g., top-hat by reconstruction, granulometry, and directionality), which are summarized as follows.

- *Brightness*: The maximum value between the visible bands for each pixel is recorded as its brightness. The visible bands are focused on since they have the most significant contribution to the spectral property of buildings [15].
- *Local contrast*: The relatively high reflectance of roofs and the spatially adjacent shadows leads to a high local contrast of buildings. Top-hat transformation is used to describe the contrast since it is able to highlight the locally bright structures with a size up to a predefined value.
- *Size*: Buildings in the high-resolution images show complicated spatial patterns with multiscale characteristics. Differential morphological profiles (DMPs) [16] are therefore used to construct the building index.
- *Directionality*: A challenging task for the construction of a building index is how to automatically filter out roads that have a very similar spectral reflectance to buildings. Roads are always elongated in one or two directions while buildings are more isotropic. Consequently, the MBI is implemented using a series of linear structural elements (SE) that are able to measure the directionality of local structures [17].

The MBI is calculated by the following steps.

Step 1) Calculation of the maximum digital number (DN). The maximum of the multispectral bands for each pixel is recorded for the subsequent processing:

$$b(i) = \max_{1 \le k \le K} \left(\mathrm{band}_k(i) \right) \tag{1}$$

where $\mathrm{band}_k(i)$ indicates the DN of pixel i for the k-th spectral band, and K is the number of multispectral bands. b represents the maximum DN image.

Step 2) DMPs of the top-hat transformation. The spectral-structural characteristics of buildings are represented using the DMPs of the top-hat transformation (TH-DMP) with multiscale and multidirectional SE, which is defined as

$$\mathrm{TH-DMP}(d,s) = \left| \mathrm{TH}_b(d,s) - \mathrm{TH}_b(d, s - \Delta s) \right|$$

with

$$\mathrm{TH}_b(d,s) = b - \gamma_b^{\mathrm{re}}(d,s) \tag{2}$$

where γ_b^{re} represents the opening-by-reconstruction [16] of the feature image b, $s(s_{\min} \le s \le s_{\max})$ and d indicate the scale and direction of a linear SE, respectively, and Δs is the interval of the profiles. It

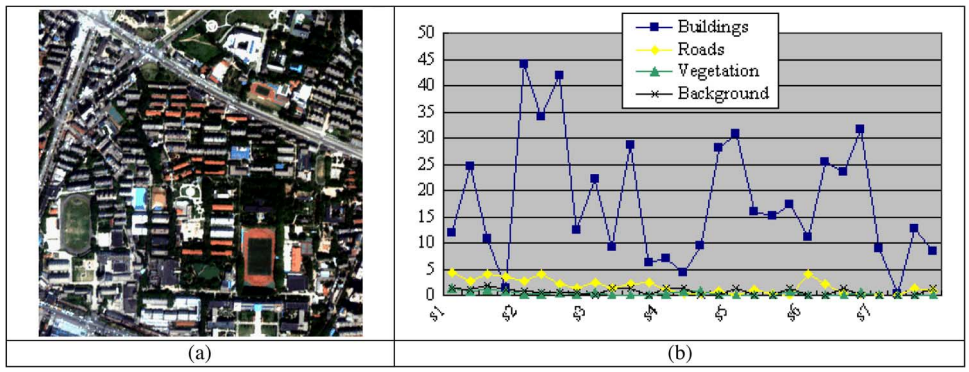

Fig. 1. Performance of the MBI: (a) is a true-color QuickBird image from Wuhan University; and (b) is the TH-DMP histogram for the main land-cover classes, where the horizontal axis represents the scale and direction of SE, and the vertical axis represents the TH-DMP feature values. The horizontal axis is labeled from scale 1 (s1) to scale 7 (s7) with four directions (45°, 90°, 135°, and 180°) at each scale.

should be noted that the scale parameter s is used to extract objects with different sizes.

Step 3) Calculation of MBI. The MBI is defined as the average of the multiscale and multidirectional TH-DMP:

$$\mathrm{MBI} = \frac{\sum_{d}\sum_{s} \mathrm{TH-DMP}(d,s)}{D \times S} \tag{3}$$

where D and S are the numbers of directionality and scale, respectively. Four directions are considered in this study ($D = 4$) since it was shown that an increase in D did not lead to an increase in accuracy of the building detection [13], [14]. The scale parameters are determined according to the sizes of the buildings and the spatial resolution of the images. The construction of MBI is based on the fact that building structures have larger values in most of the scales and directions in the TH-DMP histogram, due to their local contrast and isotropy. As a consequence, the structures with large MBI values are more likely to be buildings, and the other components are filtered out.

Fig. 1 shows the TH-DMP histogram of the main land-cover classes, including buildings, roads, vegetation and background. In Fig. 1(b), the vertical axis stands for the TH-DMP feature values, and the horizontal axis represents the scale and direction. Specifically, the scale parameters are set to $s_{\min} = 2$ and $s_{\max} = 32$ with an interval of 5 ($\Delta s = 5$). At each scale, four directions (45°, 90°, 135°, and 180°) are considered. Accordingly, four directions and seven scales lead to a 28-dimension TH-DMP feature, as shown in the horizontal axis of Fig. 1(b). It can be clearly seen that in most of the dimensions, the feature values of the TH-DMP for buildings are significantly larger than the other land-cover classes. In this way, the MBI is able to automatically highlight buildings and suppress the background, and, thus, it has the potential to indicate the change information of buildings from high-resolution imagery.

B. Conditions of Building Change

The spectral, MBI and shape conditions should be satisfied simultaneously for the identification of building change.

1) Spectral Condition (C1): Building change information is primarily related to the spectral variation. This assumption is based on the fact that the change of buildings always leads to a change in the spectral reflectance of the area where the change takes place. The spectral change magnitude is therefore used to describe the spectral variation:

$$\mathrm{SPE}(i) = \mathrm{abs}\left(b^{\mathrm{t1}}(i) - b^{\mathrm{t2}}(i)\right) \tag{4}$$

where $\mathrm{SPE}(i)$ is the spectral change value of pixel i, $\mathrm{abs}(\cdot)$ calculates the absolute value, and $b^{\mathrm{t1}}(i)$ and $b^{\mathrm{t2}}(i)$ represent the maximum DN values of pixel i at time t1 and t2, respectively. The spectral condition (C1) of building change is defined as:

$$\mathrm{SPE}(i) > \mathrm{T(SPE)} \tag{5}$$

with T(SPE) being the spectral threshold.

2) MBI Condition (C2): The spectral condition indicates the general change information for all the land-cover classes; however, target-driven change detection should be related to the characteristics of the target of interest. To this end, the MBI is used to focus on the change information of buildings. The advantages of MBI include that it is fast, effective, and unsupervised, without a requirement for the selection of training samples. In this study, the MBI condition is defined at both the feature and decision levels. At the feature-level, the difference of the multitemporal MBI feature images is directly used to indicate the change of buildings. At the decision-level, the building information in the multitemporal datasets is first extracted, and the difference in the multitemporal building information is subsequently used to detect the change of buildings. The MBI condition (C2) at the feature-level is formulated as:

$$\begin{aligned} &\mathrm{MBI}(i) > \mathrm{T(MBI)} \\ &\text{with } \mathrm{MBI}(i) = \mathrm{abs}\left(\mathrm{MBI}^{\mathrm{t1}}(i) - \mathrm{MBI}^{\mathrm{t2}}(i)\right) \end{aligned} \tag{6}$$

where MBI(i) is the MBI change value of pixel i, and $\mathrm{MBI}^{\mathrm{t1}}(i)$ and $\mathrm{MBI}^{\mathrm{t2}}(i)$ represent the MBI feature values of pixel i at

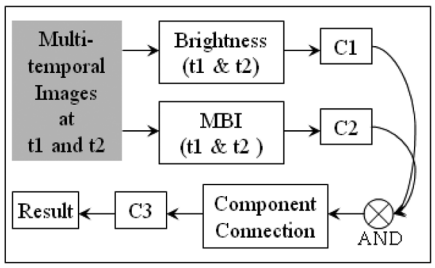

Fig. 2. Processing chain of the MBI-based automatic building change detection.

time t1 and t2, respectively. T(MBI) is the change threshold. The MBI condition (C2) at the decision-level is defined as:

$$\begin{aligned} &\mathrm{B}(i) = \left(\mathrm{B}^{\mathrm{t}1}(i) - \mathrm{B}^{\mathrm{t}2}(i)\right) \neq 0 \\ &\text{with} \begin{cases} \mathrm{B}^{\mathrm{t}1}(i) = 1 \\ \mathrm{B}^{\mathrm{t}2}(i) = 1 \end{cases} \text{for} \begin{cases} \mathrm{MBI}^{\mathrm{t}1}(i) \geq \mathrm{T(MBI)} \\ \mathrm{MBI}^{\mathrm{t}2}(i) \geq \mathrm{T(MBI)} \end{cases} \\ &\text{otherwise} \begin{cases} \mathrm{B}^{\mathrm{t}1}(i) = 0 \\ \mathrm{B}^{\mathrm{t}2}(i) = 0 \end{cases} \end{aligned} \tag{7}$$

where $\mathrm{B}(i)$ stands for the change of buildings, and $\mathrm{B}^{\mathrm{t}1}(i)$ and $\mathrm{B}^{\mathrm{t}2}(i)$ represent the detected building information at time t1 and t2, respectively.

3) Shape Condition (C3): The shape condition is used to reduce false alarms by removing irregular structures such as road-like narrow objects. The assumption of the shape condition is that the changed building structures should satisfy the basic shape properties of buildings, such as rectangularity and size. It should be noted that the shape is considered as a post-filter and cannot be used before the spectral and MBI conditions. This is because the shape information alone is not adequate to identify the presence or change of buildings, and a blind use of shape or semantic conditions might lead to a low accuracy of information extraction [18]. Furthermore, the shape condition is carried out based on image objects instead of pixels. Consequently, before its implementation, the objects that indicate the changed building areas are primarily formed by labeling the connected components. Connected component labeling [19] is carried out by scanning an image, pixel-by-pixel, in order to identify connected pixel regions, i.e., regions of adjacent pixels which share the same intensity value. Specifically, in this study, the spatially adjacent building change pixels are connected with the 8-connectivity approach. In this way, shape attributes can be extracted from the objects, and the shape condition (C3) is defined as:

$$\mathrm{Area}(obj) > \mathrm{T(A)}\ \mathrm{AND}\ \mathrm{GI}(obj) > \mathrm{T(G)} \tag{8}$$

where $\mathrm{Area}(\cdot)$ stands for the area of the object obj, and $\mathrm{GI}(\cdot)$ represents the geometrical index (GI) [14] of the buildings:

$$\mathrm{GI} = a \cdot \frac{\text{Rectangular Fit}}{\text{Length} - \text{Width Ratio}} \tag{9}$$

where a is a coefficient used to adjust the range of the GI values, and it is normally set to 10. T(A) and T(G) are the thresholds for the area and GI, respectively. The area stands for the number of pixels in an object, and it is used to remove small noise. The GI is defined as the ratio between the rectangular fit and the length-width ratio. The rectangular fit is defined based on the creation of a rectangle with the same area as the considered object. It is calculated by comparing the number of pixels inside the rectangle and the total number of pixels for the considered object. A building object is expected to have a large GI since it is usually related to a high rectangular fit and a small length-width ratio. The GI is able to suppress irregular and narrow structures that are apparently not buildings. Definiens [20] software is used to generate the rectangular fit and the length-width ratio as the inputs of the shape condition.

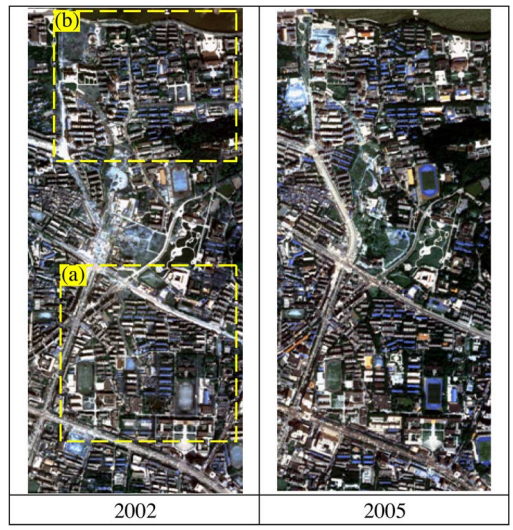

Fig. 3. The RGB true-color QuickBird image pairs from 2002 and 2005 over Hongshan District, Wuhan, central China. The two subset images (a) and (b) are highlighted with two rectangular frames.

C. MBI-Based Building Change Detection

Based on the aforementioned conditions, two novel building change detection algorithms are proposed at the feature-level and decision-level, respectively.

The processing chain of the MBI automatic building change detection is shown in Fig. 2. It should be kept in mind that C2 is related to the feature-level or decision-level. The processing steps are described as follows.

Step 1) Preprocessing: The multitemporal images are radiometrically corrected and co-registered. The registration process is implemented by the use of a polynomial function of the second order, according to a series of carefully chosen ground control points.

Step 2) Calculation of the multitemporal feature images: The brightness images and the MBI images at time t1 and t2 are calculated, respectively. All the feature images are linearly scaled into the range of 0 to 1.

Step 3) C1 and C2: The image structures that simultaneously satisfy the spectral and MBI conditions are labeled as the candidate change components of buildings.

Step 4) Component connection: The objects of changed buildings are formed by connecting the spatially adjacent changed components that are generated by *Step3*.

Step 5) Shape filtering: The GI and area attributes are used to reduce the false alarms in the results.

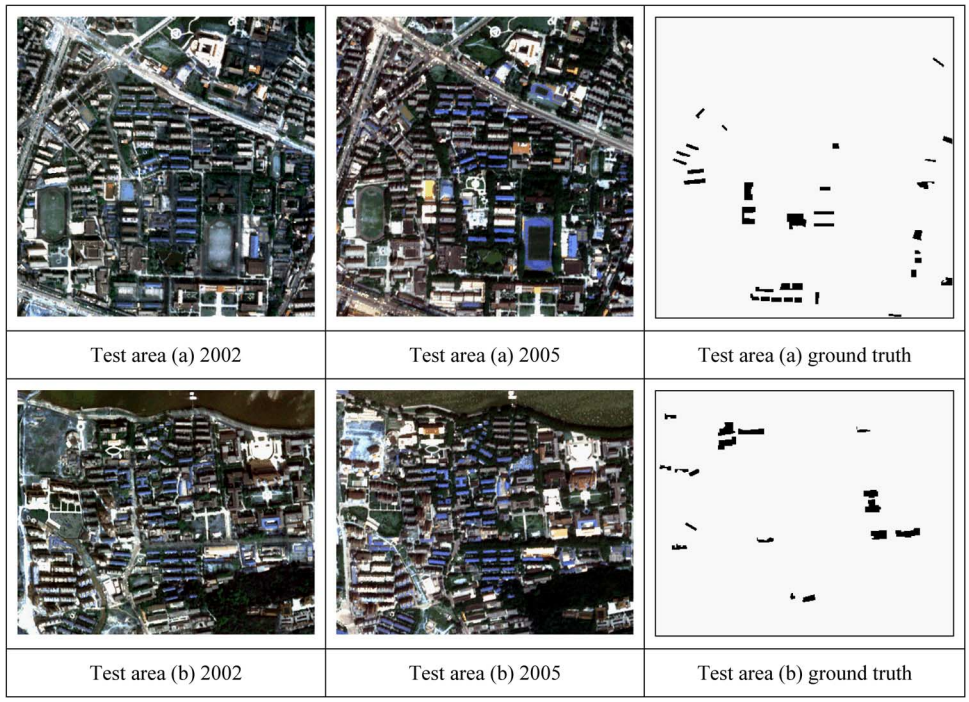

Fig. 4. The two subsets and their ground truth maps of building change used for the evaluation of the proposed algorithms. The first and second rows display the datasets of test areas (a) and (b), respectively. In the ground truth maps, the black patches indicate the changed buildings while the white color indicates unchanged areas.

The processing chain can be easily embedded into an urban information management system and can be used to rapidly detect building change information from high-resolution imagery. It can help to significantly alleviate the burdensome manual work of delineating changed buildings from a remote sensing image database.

III. Datasets

The analysis of the building change detection is carried out based on a pair of QuickBird multispectral images acquired in 2002 and 2005, as shown in Fig. 3. Both the images include three visible spectral bands and one near-infrared band, with a spatial resolution of 2.4 m. A total of 15 ground control points were chosen for the co-registration of the multitemporal image pairs, resulting in a residual misregistration of less than 1 pixel. The study area lies in the Hongshan District of Wuhan City, and covers approximately 1.2 km by 2.7 km. It is a typical urban landscape of China, where dense residential and commercial areas are mixed together. Due to the rapid infrastructure construction and updating in this rapidly developing country, the study area shows complicated land-cover change.

In order to effectively evaluate the building change detection algorithms, two subsets were chosen from the study area, with a field campaign generating two manually delineated ground truth maps of building change, as presented in Fig. 4. In the study area, the changed buildings refer to both newly built and rebuilt ones. The main challenge lies in that the roads and bright soil may lead to false alarms due to their similar spectral properties to buildings. Furthermore, the different acquisition conditions at the two dates and the residential registration noise also result in a large number of false alarms.

IV. Experimental Results

In this section, the performance of the different change conditions (spectral, MBI, and shape) is reported, and the discussion is divided into two parts: feature-level and decision-level. The sensitivity of parameters is also analyzed. The experiment setup is summarized as follows.

1) Combination of change conditions
   - MBI condition only (C2)
   - $\mathrm{MBI} + \mathrm{spectral}(\mathrm{C1} + \mathrm{C2})$
   - $\mathrm{MBI} + \mathrm{spectral} + \mathrm{shape}(\mathrm{C1} + \mathrm{C2} + \mathrm{C3})$
2) Parameters
   - The thresholds of the spectral condition T(SPE) are 0.1, 0.2, and 0.3.
   - The thresholds of the MBI condition T(MBI) for both feature and decision levels are from 0.1 to 0.9, with an interval of 0.1.
   - The thresholds of the shape condition are set to $\mathrm{T(A)} = 30$ pixels and $\mathrm{T(G)} = 2.0$, according to our previous experiments [13], [14] and the spatial characteristics of the buildings in the study area.
3) Accuracy evaluation

   Four indexes are used to evaluate the accuracy of the building change detection by comparing the detection results and the ground truth map:
   - Correctness (%) =# (correctly detected changed buildings)/# (changed buildings)>
   - False alarms (%) =# (incorrectly detected /changed buildings)# (background)
   - Missed alarms (%) =# (missed changed buildings)/ # (changed buildings)

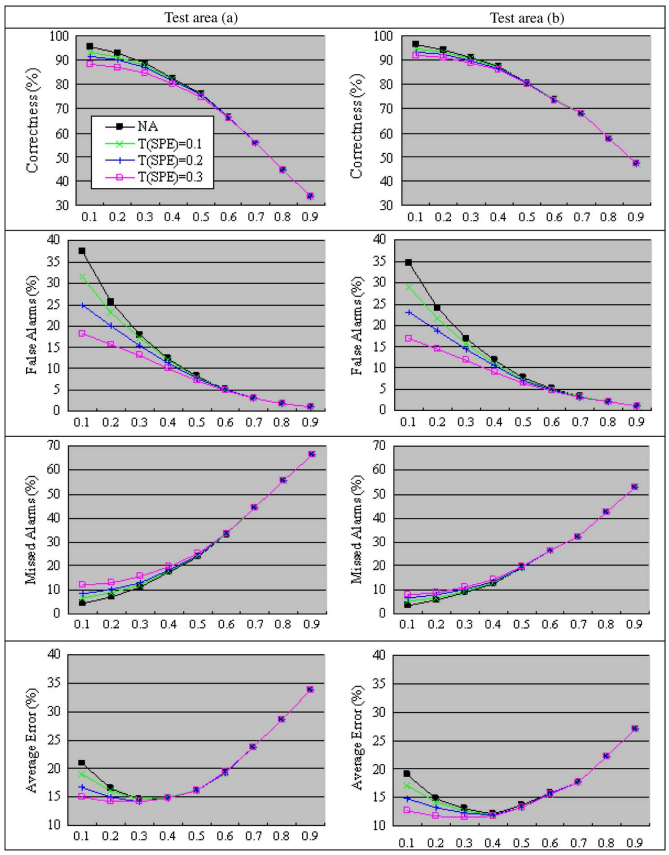

Fig. 5. Accuracies of the proposed building change detection at the feature-level with C2 and C1 + C2 for test area (a) (left column) and area (b) (right column). All the charts share the same legend, which is displayed only once in the left-upper chart. The horizontal axis represents the MBI threshold T(MBI). 'NA' in the legend means that the spectral condition is not used.

- Average error (%) = (false alarms + missed alarms)/2

The background includes unchanged buildings and other land-cover classes that are not of interest in this study. The average error defined in this paper indicates the overall error and a balance between the omission and commission errors. It should be noted that the average error can be used to estimate the operation intensity of manual work that is required to correct the omission and commission errors derived from the computer-based processing.

A. Results at the Feature-Level

The accuracies of C2 and C1 + C2 at the feature-level for the two subsets are shown in Fig. 5, where 'NA' means the spectral condition is not considered. The observations can be summarized as follows.

1) General trend: The correctness rate and the false alarms decrease and the missed alarms increase gradually with increasing values of T(MBI) since more components have been removed with a larger change threshold. The curves of the average error show that there is a tradeoff between the false alarms and missed alarms, and it can be seen that the balance point or the appropriate threshold is around $\mathrm{T(MBI)} = 0.3$.

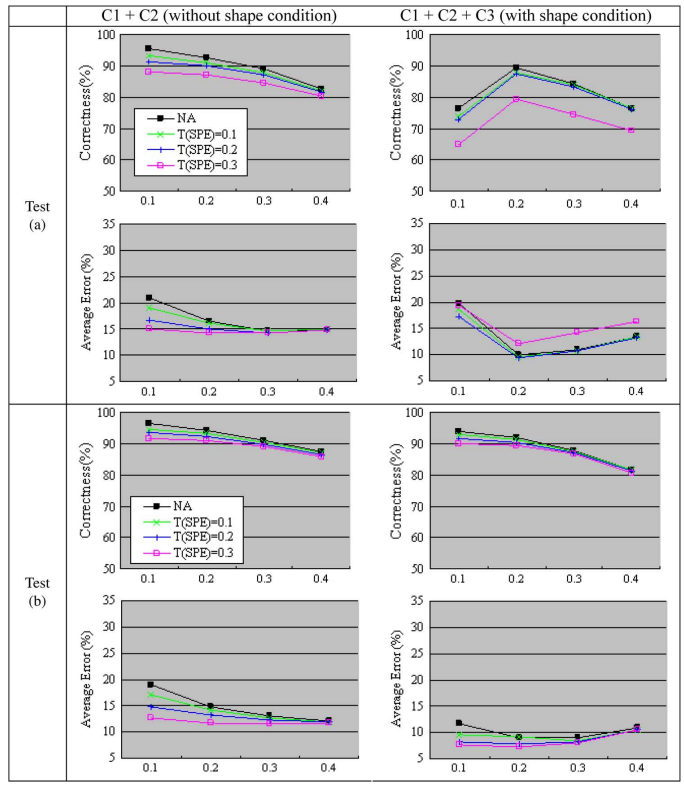

Fig. 6. Influence of the shape condition for the building change detection at the feature-level for test areas (a) and (b). The left and right columns represent the accuracies without and with the shape condition, respectively. The horizontal axis represents the MBI threshold T(MBI) from 0.1 to 0.4, with an interval of 0.1.

Effects of the spectral condition: By analyzing the results with different spectral thresholds T(SPE), it can be seen that the spectral condition is able to effectively reduce the false alarms and average errors but at the same time maintain the correctness rate. However, the influence of the spectral condition weakens gradually when the value of T(MBI) becomes larger.

When the shape condition is considered, the results are presented in Fig. 6 for both test areas (a) and (b). In both datasets, the left and right columns show the accuracies without and with the shape constraint, respectively. It should be noted that only the results with $\mathrm{T(MBI)} = 0.1, 0.2, 0.3,$ and 0.4 are reported because the other results cannot give a satisfactory correctness rate (less than 80%). From the figures, it can be seen that the addition of the shape condition leads to a reduction in the correctness rate, to some extent. The reduction in test area (a) is more apparent than in test (b), but, at the same time, their average errors also decrease significantly. It can be stated that with the shape constraints the average error is reduced at the cost of a decrease for the correctness rate. In this experiment, the parameters of $\mathrm{T(MBI)} = (0.2, 0, 3)$ and $\mathrm{T(SPE)} = (\mathrm{NA}, 0.1, \text{and } 0.2)$ generate satisfactory results since they maintain the correctness rate and simultaneously achieve the lowest average error.

B. Results at the Decision-Level

The accuracies of C2 and C1 + C2 at the decision-level for the two subsets are shown in Fig. 7. It can be seen that the accuracy curves of test areas (a) and (b) show similar trends. The

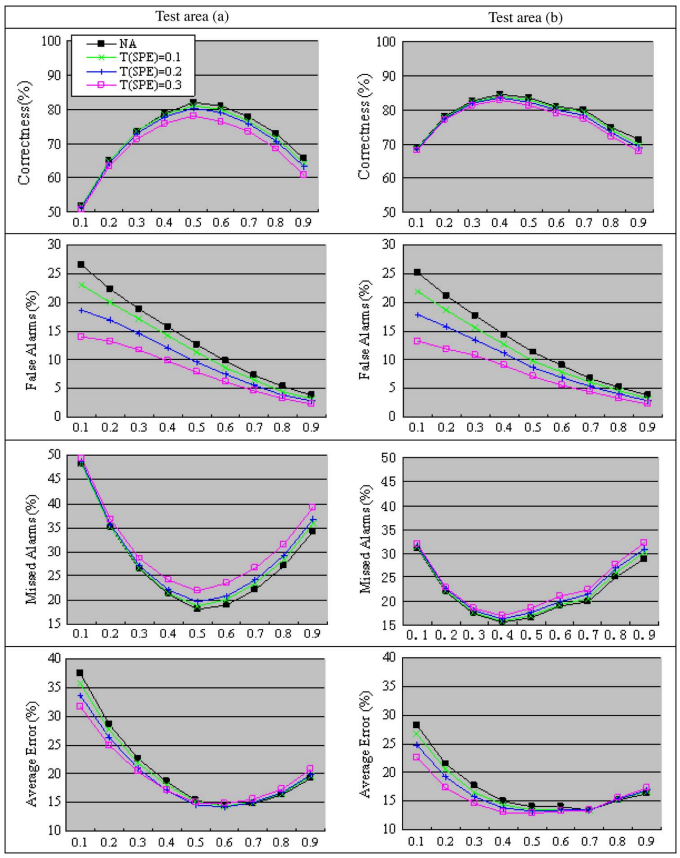

Fig. 7. Accuracies of the proposed building change detection at the decision-level with C2 and C1 + C2 for test area (a) (left column) and area (b) (right column). All the charts share the same legend, which is displayed only once in the left-upper chart. The horizontal axis represents the MBI threshold T(MBI) from 0.1 to 0.9, with an interval of 0.1.

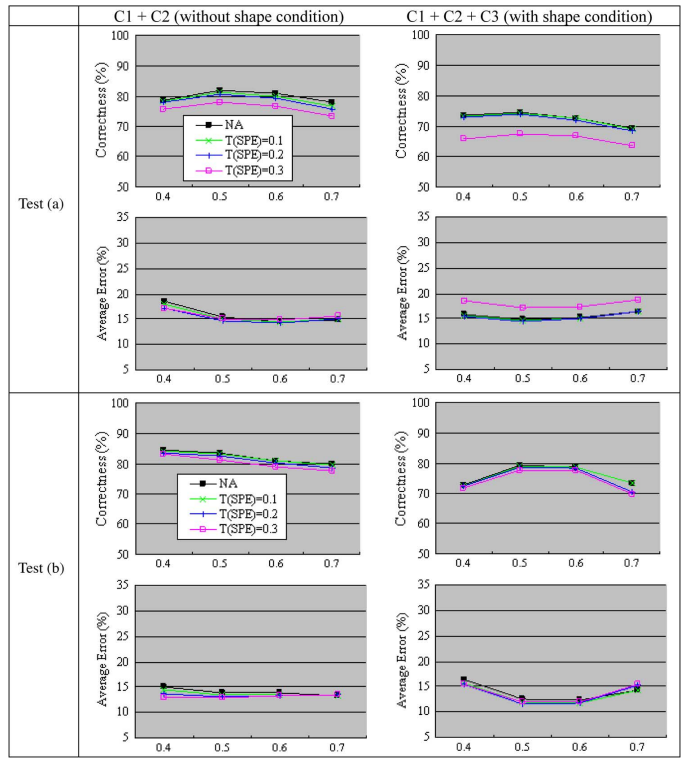

Fig. 8. Influence of the shape condition for the building change detection at the decision-level for test areas (a) and (b). The left and right columns represent the accuracies without and with the shape condition, respectively. The horizontal axis represents the MBI threshold T(MBI) from 0.4 to 0.7, with an interval of 0.1.

first observation regarding the decision-level change detection is that it cannot achieve comparable correctness rates to the feature-level approach, since the highest correctness rates for the feature-level detection are 95.5% and 96.4% for test areas (a) and (b), respectively, but the highest correctness rates for the decision-level approach are 81.9% and 84.4%, respectively. It can be attributed to the fact that the decision-level change detection relies on the binarization of the multitemporal MBI images, leading to information loss for building change. An appropriate range for the T(MBI) is between 0.4 and 0.7 as they give relatively high correctness rates and low average errors. With respect to the threshold of the spectral condition, it can be seen that with an increasing value of T(SPE), the correctness rates decrease but the average errors are also reduced, which is similar to the results observed in the feature-level detection.

When the shape condition is taken into account, the results are presented in Fig. 8 for test area (a) and (b). Only the results with $\mathrm{T(MBI)} = 0.4$, 0.5, 0.6, and 0.7 are reported since the other parameters do not yield satisfactory correctness rates (less than 75%). From Fig. 8, it can be seen that the addition of the shape condition significantly decreases the correctness rates by an average of 5%. For the case of $\mathrm{T(SPE)} = 0.3$, the correctness rate decreases by 10%. However, on the other hand, the average errors do not show an obvious reduction. From the results of test area (b), it can also be found that the decrease in correctness rate is greater than the reduction in average error when the shape condition is considered. Although the decision-level building change detection does not achieve a satisfactory performance compared to the feature-level, it is able to yield acceptable results if the parameters are appropriately chosen. For instance, it gives a correctness rate of 75% and an average error of 15% for test area (a), and a correctness rate of 80% and an average error of 12% for test area (b), with $\mathrm{T(MBI)} = 0.5$ and 0.6.

C. Visual Inspection

In Figs. 9 and 10, a series of three-color maps are used to show the influence of the spectral, MBI, and shape conditions for test areas (a) and (b), respectively. Each color map is generated by superimposing the detection results of $\mathrm{T(SPE)} = 0.1$, 0.2 and 0.3 as red, green and blue bands, respectively. Specifically, the black color shows unchanged areas, and the red, green, and blue colors represent the changed buildings that are detected at $\mathrm{T(SPE)} = 0.1$, 0.2, and 0.3, respectively. The yellow, cyan, and magenta colors indicate the changed buildings detected by two of the three spectral thresholds, i.e., (0.1, 0.2), (0.2, 0.3), and (0.1, 0.3), respectively. The white color represents the changed buildings that are identified by all three spectral thresholds. From the figures, it can be clearly seen that the smaller spectral and MBI thresholds lead to higher correctness rates but more false alarms. On the other hand, larger thresholds correspond to lower correctness rates but fewer false alarms. This phenomenon is natural since more changed components

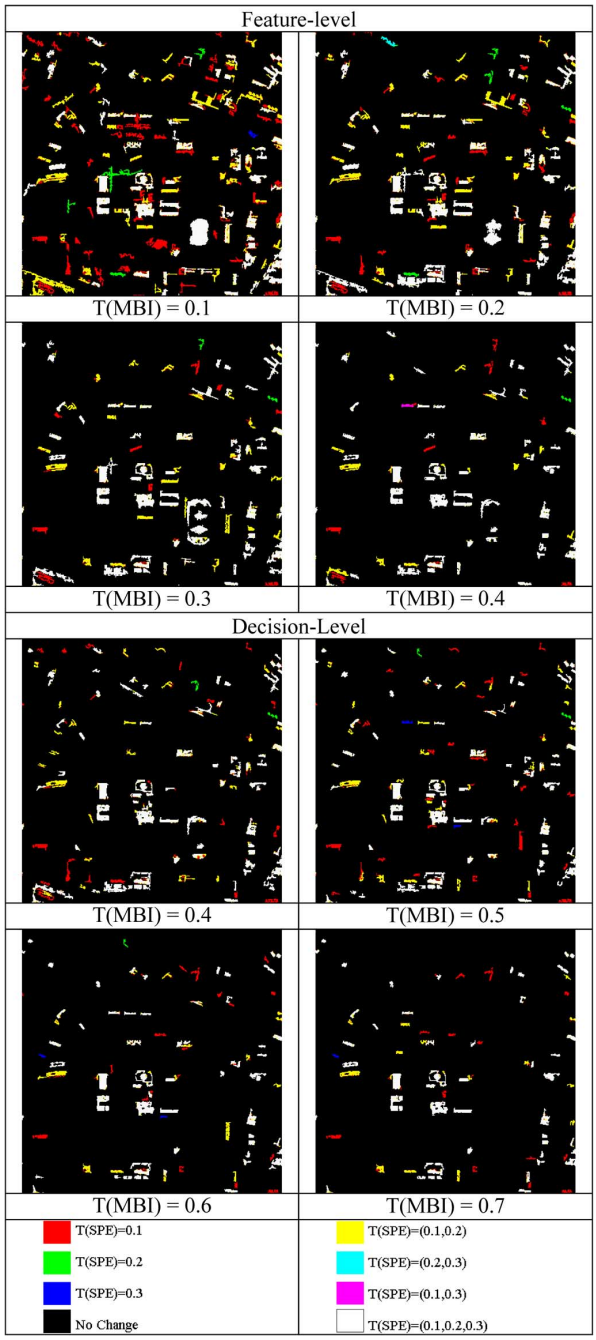

Fig. 9. Changed building maps of study area (a) at both the feature and decision levels with different parameters. All the maps are generated by the spectral, MBI, and shape conditions $(C1 + C2 + C3)$. A series of three-color maps are used to show the influence of the spectral thresholds by superimposing the detection results of $T(SPE) = 0.1$, 0.2 and 0.3 as the red, green and blue bands, respectively. Specifically, the black color shows unchanged areas, and the red, green, and blue colors represent the changed buildings that are only detected by $T(SPE) = 0.1$, 0.2, and 0.3, respectively. The yellow, cyan, and magenta colors indicate the changed buildings detected by two spectral thresholds, such as (0.1, 0.2), (0.2, 0.3), and (0.1, 0.3), respectively. The white color represents the changed buildings that are identified by all three spectral thresholds.

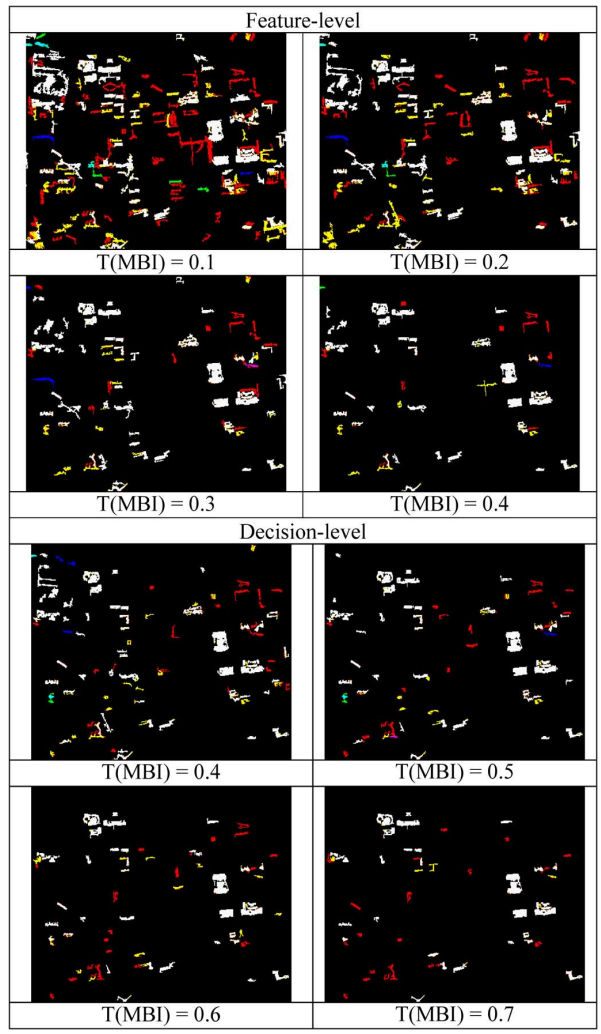

Fig. 10. Changed building maps of study area (b) at both the feature and decision levels with different parameters. All the maps are generated by the spectral, MBI, and shape conditions $(C1 + C2 + C3)$. A series of three-color maps are used to show the influence of the spectral thresholds by superimposing the detection results of $T(SPE) = 0.1$, 0.2 and 0.3 as the red, green and blue bands, respectively. The legend is the same as Fig. 9.

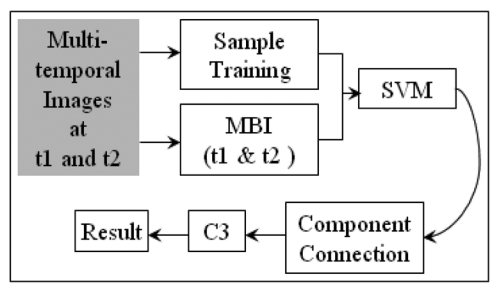

Fig. 11. The processing flowchart of the SVM-based building change detection method.

are detected by a small change threshold. In this case, the correctness rates increase at the cost of an increase in the false alarms. There is, therefore, a tradeoff between correctness rate and false alarms, and it is controlled by the change thresholds. However, it should be noted that although large thresholds do not give the highest correctness rates, they are able to visually indicate most of the building change information with fewer false alarms. This is meaningful for alleviating human labor since current building change detection is entirely reliant on human interpretation.

TABLE I
AN ACCURACY COMPARISON FOR THRESHOLD-BASED AND SVM-BASED BUILDING CHANGE DETECTION ALGORITHMS

	Method	Correctness (%)	False alarms (%)	Missed alarms (%)	Average error (%)
Test area (a)	Feature-level	87.3	6.0	12.7	9.4
	Decision-level	73.8	2.6	26.2	14.4
	MBI-SVM without C3	80.3	7.9	19.7	13.8
	MBI-SVM with C3	77.5	3.1	22.5	12.8
Test area (b)	Feature-level	90.2	5.7	9.8	7.8
	Decision-level	78.7	1.9	21.3	11.6
	MBI-SVM without C3	87.6	7.5	12.4	10.0
	MBI-SVM with C3	79.5	2.2	20.5	11.4

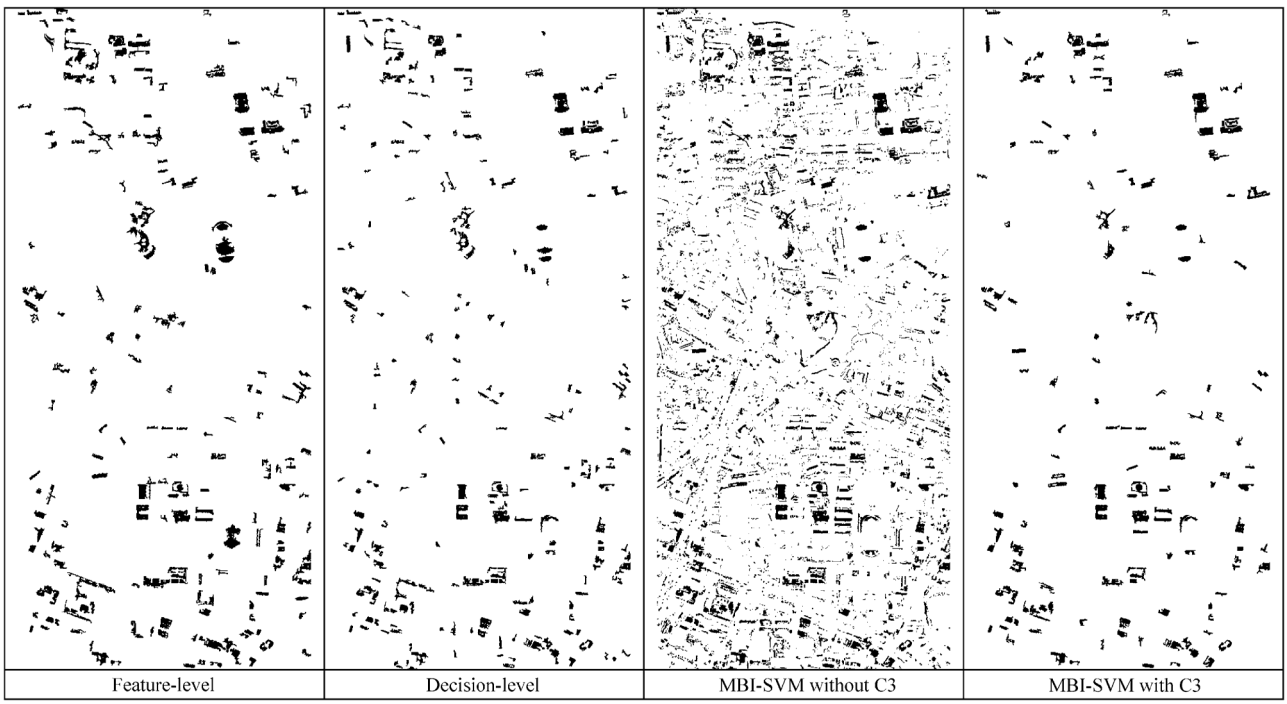

Fig. 12. Comparison between the proposed building change detection methods and the MBI-SVM algorithm. The parameters of the feature-level and decision-level methods are set as: $[\mathrm{T(SPE)}, \mathrm{T(MBI)}] = [0.3, 0.2]$ and $[\mathrm{T(SPE)}, \mathrm{T(MBI)}] = [0.3, 0.4]$, respectively. Black components represent changed buildings and the white color indicates the background.

D. Comparison

In order to validate the proposed feature-level and decision-level change detection algorithms, support vector machine (SVM) is used to interpret the multitemporal MBI feature images and produce the building change maps for comparison (noted as the MBI-SVM). The processing flowchart is shown in Fig. 11. In this comparative experiment, 100 training samples in pixels are randomly selected from the ground truth for the changed buildings and background, respectively. The radial basis function (RBF) function is used as the SVM kernel, and its parameters are chosen manually ($\mathrm{penalty\ parameter} = 100$, and the Gamma parameter of the RBF kernel is set to 0.5). SVM is used as a benchmark in order to test whether the proposed method is able to achieve comparable performance to the supervised change detection approach via machine learning.

The quantitative accuracies of the feature-level, decision-level, and the MBI-SVM algorithms are compared in Table I for both test areas (a) and (b). Their change detection maps over the whole study area (Hongshan District, Wuhan) are displayed in Fig. 12 for a visual inspection. The following observations can be obtained:

1) The shape filtering is able to significantly reduce the false alarms (e.g., noise and road-like narrow structures) of the MBI-SVM algorithm by 4.8% and 5.3% for test areas (a) and (b), respectively, but at the cost of a decrease in the correctness rate of 2.8% and 8.1%.
2) The feature-level algorithm provides a higher correctness rate and a lower average error than the decision-level and MBI-SVM algorithms. The decision-level change detection achieves comparable accuracies to the MBI-SVM.

The above results show that the threshold-based approaches are able to effectively indicate the building change information from high-resolution imagery. The results of both the visual inspection and the quantitative accuracies can be considered as satisfactory, even when compared to the SVM-based machine learning algorithm.

V. Conclusion

The contribution of this study is to propose a novel building change detection method for multitemporal high-resolution imagery. The basic idea of the method is to indicate the building change information based on the difference of the multitemporal morphological building index (MBI) at feature or decision-level. The characteristic of the proposed method is that it is implemented without any training samples, but it is able to achieve higher correctness rates and lower average errors than the SVM-based supervised algorithm. It should be kept in mind that automatic building change detection from complicated urban landscapes using high-resolution imagery is a challenging task due to the spectral confusion between roads, buildings and other ground materials, and the geometrical differences between multitemporal high-resolution images caused by different view angles. Although the proposed algorithms are subject to several parameters, including the thresholds of spectral and MBI change, they do not require the selection of training samples and, hence, they have the potential to replace the current urban building change detection methods, which are totally reliant on human visual interpretation. In addition, according to the parameter sensitivity analysis conducted in this study, the appropriate parameters are suggested as $\mathrm{T(MBI)} = (0.2, 0.3)$, and $\mathrm{T(SPE)} = (0.1, 0.2, 0.3)$ for the feature-level change detection approach (The MBI feature images are linearly scaled into the range from 0 to 1).

The effectiveness of the proposed algorithm has been validated on QuickBird images (2002 and 2005) of Hongshan District of Wuhan City in central China. The study area is a typical Chinese urban area with different kinds of urban building change, including construction, updating and removal. The main experimental results are summarized as follows:

1) In terms of quantitative accuracies, the feature-level detection gave significantly higher correctness rates and lower overall errors than the decision-level algorithm, while the decision-level detection achieved comparable results to the machine learning change detection by SVM.
2) From the visual interpretation point of view, most of the changed buildings were labeled by the three algorithms (i.e., the threshold-based and the MBI-SVM methods). In particular, the feature/decision-level algorithms with larger thresholds generated satisfactory visual results since the false alarms were significantly suppressed. It can therefore be stated that the proposed algorithms are able to reduce the human labor that is required for the current building change detection systems.

References

[1] L. Gueguen, P. Soille, and M. Pesaresi, "Change detection based on information measure," *IEEE Trans Geosci. Remote Sens.*, vol. 49, no. 11, pp. 4503–4515, Nov. 2011.

[2] X. Huang, L. Zhang, and P. Li, "Classification and extraction of spatial features in urban areas using high resolution multispectral imagery," *IEEE Geosci. Remote Sens. Lett.*, vol. 4, no. 2, pp. 260–264, Apr. 2007.

[3] F. Bovolo, L. Bruzzone, and S. Marchesi, "Analysis and adaptive estimation of the registration noise distribution in multitemporal VHR images," *IEEE Trans Geosci. Remote Sens.*, vol. 47, no. 8, pp. 2658–2671, Aug. 2009.

[4] J. Im, J. R. Jensen, and J. A. Tullis, "Object-based change detection using correlation image analysis and image segmentation," *Int. J. Remote Sens.*, vol. 29, no. 2, pp. 399–423, Jan. 2008.

[5] F. Bovolo, "A multilevel parcel-based approach to change detection in very high resolution multitemporal images," *IEEE Geosci. Remote Sens. Lett.*, vol. 6, no. 1, pp. 33–37, Jan. 2009.

[6] S. Berberoglu, A. Akin, P. M. Atkinson, and P. J. Curran, "Utilizing image texture to detect land-cover change in Mediterranean coastal wetlands," *Int. J. Remote Sens.*, vol. 31, no. 11, pp. 2793–2815, Jun. 2010.

[7] M. Dalla Mura, J. A. Benediktsson, F. Bovolo, and L. Bruzzone, "An unsupervised technique based on morphological filters for change detection in very high resolution images," *IEEE Geosci. Remote Sens. Lett.*, vol. 5, no. 3, pp. 433–437, Jul. 2008.

[8] E. Pagot and M. Pesaresi, "Systematic study of the urban postconflict change classification performance using spectral and structural features in a support vector machine," *IEEE J. Sel. Topics Appl. Earth Obs. Remote Sens.*, vol. 1, no. 2, pp. 120–128, Jun. 2008.

[9] L. D. Robertson and D. J. King, "Comparison of pixel- and object-based classification in land cover change mapping," *Int. J. Remote Sens.*, vol. 32, no. 6, pp. 1505–1529, Mar. 2011.

[10] F. Pacifici, F. Del Frate, C. Solimini, and W. J. Emery, "An innovative neural-net method to detect temporal changes in high-resolution optical satellite imagery," *IEEE Trans Geosci. Remote Sens.*, vol. 45, no. 9, pp. 2940–2952, Sep. 2007.

[11] M. Chini, F. Pacifici, W. J. Emery, N. Pierdicca, and F. Del Frate, "Comparing statistical and neural network methods applied to very high resolution satellite images showing changes in man-made structures at rocky flats," *IEEE Trans Geosci. Remote Sens.*, vol. 46, no. 6, pp. 1812–1821, Jun. 2008.

[12] F. Pacifici and F. Del Frate, "Automatic change detection in very high resolution images with pulse-coupled neural networks," *IEEE Geosci. Remote Sens. Lett.*, vol. 7, no. 1, pp. 58–62, Jan. 2010.

[13] X. Huang and L. Zhang, "A multidirectional and multiscale morphological index for automatic building extraction from multispectral GeoEye-1 imagery," *Photogramm. Eng. Remote Sens.*, vol. 77, no. 7, pp. 721–732, Jul. 2011.

[14] X. Huang and L. Zhang, "Morphological building/shadow index for building extraction from high-resolution imagery over urban areas," *IEEE J. Sel. Topics Appl. Earth Obs. Remote Sens.*, vol. 5, no. 1, pp. 161–172, Feb. 2012.

[15] M. Pesaresi, A. Gerhardinger, and F. Kayitakire, "A robust built-up area presence index by anisotropic rotation-invariant textural measure," *IEEE J. Sel. Topics Appl. Earth Obs. Remote Sens.*, vol. 1, no. 3, pp. 180–192, Sep. 2008, 2008.

[16] M. Pesaresi and J. A. Benediktsson, "A new approach for the morphological segmentation of high-resolution satellite imagery," *IEEE Trans Geosci. Remote Sens.*, vol. 39, no. 2, pp. 309–320, Feb. 2001.

[17] P. Soille and H. Talbot, "Directional morphological filtering," *IEEE Trans. Pattern Anal. Mach. Intell.*, vol. 23, no. 11, pp. 1313–1329, Nov. 2001.

[18] X. Huang and L. Zhang, "An SVM ensemble approach combining spectral, structural, and semantic features for the classification of high-resolution remotely sensed imagery," *IEEE Trans. Geosci. Remote Sens.*, vol. 51, no. 1, pp. 257–272, Jan. 2013.

[19] R. C. Gonzalez and R. E. Woods, *Digital Image Processing*, 2nd ed. Upper Saddle River, NJ, USA: Prentice Hall, 2002.

[20] *"Definiens Developer 7, Reference Book,"* Definiens AG, Munich, Germany, 2007.

Xin Huang (M'12) received the Ph.D. degree in Photogrammetry and Remote Sensing at the State Key Laboratory of Information Engineering in Surveying, Mapping and Remote Sensing (LIESMARS), Wuhan University, Wuhan, China, in 2009.

He is currently an Associate Professor at the LIESMARS, Wuhan University. His research interests include hyperspectral data analysis, high resolution image processing, pattern recognition and remote sensing applications. He has published more than 30 peer-reviewed articles in international journals such as IEEE Transactions on Geoscience and Remote Sensing, IEEE Geoscience and Remote Sensing Letters, IEEE Journal of Selected Topics in Applied Earth Observations and Remote Sensing, Photogrammetric Engineering and Remote Sensing and International Journal of Remote Sensing.

Dr. Huang has served as a Reviewer for most of the international journals for remote sensing. He was the recipient of the Top-Ten Academic Star of Wuhan University in 2009. In 2010, he received the Boeing Award for the best paper

in image analysis and interpretation from the American Society for Photogrammetry and Remote Sensing. In 2011, he was the recipient of the New Century Excellent Talents in University from the Ministry of Education of China. In 2011, he was recognized by the IEEE Geoscience and Remote Sensing Society as the Best Reviewer of IEEE GEOSCIENCE AND REMOTE SENSING LETTERS. In 2012, he was the recipient of the National Excellent Doctoral Dissertation Award of China.

Liangpei Zhang (M'06–SM'08) received the B.S. degree in physics from Hunan Normal University, ChangSha, China, in 1982, the M.S. degree in optics from the Xi'an Institute of Optics and Precision Mechanics of Chinese Academy of Sciences, Xi'an, China, in 1988, and the Ph.D. degree in photogrammetry and remote sensing from Wuhan University, Wuhan, China, in 1998.

He is currently with the State Key Laboratory of Information Engineering in Surveying, Mapping and Remote Sensing, Wuhan University, as the head of the Remote Sensing Division. He is also a Chang-Jiang Scholar Chair Professor appointed by the Ministry of Education, China. He is currently the Principal Scientist for the China State Key Basic Research Project (2011–2016) appointed by the Ministry of National Science and Technology of China to lead the remote sensing program in China. He is an Executive Member (Board of Governor) of the China National Committee of International Geosphere-Biosphere Programme.

Dr. Zhang also serves as an Associate Editor of *International Journal of Ambient Computing and Intelligence*, *International Journal of Image and Graphics*, *International Journal of Digital Multimedia Broadcasting*, *Journal of Geo-spatial Information Science*, and the *Journal of Remote Sensing*. He has more than 260 research papers and is the holder of 5 patents. His research interests include hyperspectral remote sensing, high resolution remote sensing, image processing and artificial intelligence. He is a fellow of the Institution of Electrical Engineers, an executive Member for the China Society of Image and Graphics, and others. He regularly serves as a Cochair of the series SPIE Conferences on Multispectral Image Processing and Pattern Recognition, Conference on Asia Remote Sensing, and many other conferences. He edits several conference proceedings, issues, and the Geoinformatics Symposiums. He is currently serving as an Associate Editor for the IEEE TRANSACTIONS ON GEOSCIENCE AND REMOTE SENSING.

Tingting Zhu received the B.S. degree from Nanjing Normal University, Nanjing, China, in 2012. She is currently pursuing the M.S. degree at the State Key Laboratory of Information Engineering in Surveying, Mapping, and Remote Sensing (LIESMARS), Wuhan University, Wuhan, China.

Her research interests include change detection from high-resolution remotely sensed imagery.